Nuclear Instruments and Methods in Physics Research A 1089 (2026) 171585

Contents lists available at ScienceDirect

Nuclear Inst. and Methods in Physics Research, A

journal homepage: www.elsevier.com/locate/nima

Full Length Article

Axion–nucleon sensitivity using ultra-low background Micromegas detectors for the International Axion Observatory

I. Antolín [a,b,*], J.F. Castel [a], T. Dafni [a], E. Ferrer-Ribas [c], J. Galán [a], A. Huerva [a,**], I.G. Irastorza [a], G. Luzón [a], C. Margalejo [a], H. Mirallas [a], L. Obis [a], J. Porrón [a], M.J. Puyuelo [a], J. Ruz [d,a,***], J.K. Vogel [d,a]

[a] Centro de Astropartículas y Física de Altas Energías (CAPA) & Departamento de Física Teórica, Universidad de Zaragoza, 50009 Zaragoza, Spain
[b] Institute of Experimental Physics. University of Hamburg, Luruper Chaussee 149 22761, Hamburg, Germany
[c] IRFU, CEA, Université Paris-Saclay, 91191 Gif-sur-Yvette, France
[d] Fakultät für Physik. Technische Universität Dortmund., Dortmund, D-44221, Germany

ARTICLE INFO

Keywords:
Axions
Dark matter
Helioscopes
Micromegas
IAXO

ABSTRACT

The International Axion Observatory (IAXO) aims to detect ultra-light bosonic dark matter candidates by combining strong magnetic fields, X-ray optics, and ultra-low background detectors. This work investigates the efficiency and sensitivity of various Micromegas detector configurations within IAXO, with a particular focus on the challenging axion–nucleon coupling channel. Through detailed simulations, we evaluate the intrinsic efficiency of the IAXO-D1 prototype, exploring both conventional argon-isobutane gas mixtures and a custom blend composed of 48.85% xenon, 48.85% neon, and 2.3% isobutane, under different pressure conditions. Detector responses are studied across a range of axion spectra. To support this analysis, a dedicated simulation framework was developed by integrating the Rare Event Searches Toolkit (REST) with Garfield++, Magboltz, and Geant4. The results highlight that Micromegas detectors operated with the xenon–neon-based gas mixture exhibit a marked improvement in performance compared to the nominal IAXO-D1 baseline configuration, with a signal-to-noise ratio enhancement of up to a factor of 3.7 in the case of axion–nucleon coupling sensitivity.

1. Introduction

The axion is a hypothetical elementary pseudo-scalar particle that was originally postulated by R. Peccei and H. Quinn (PQ) [1,2] to address the strong CP problem. Axions and similar particles, like the more generic pseudo-scalar bosonic Axion-Like Particles (ALPs) [3,4], can have a wide range of possible masses and coupling strengths, leading to a large parameter space that will be explored by experiments such as the International Axion Observatory (IAXO) [5], a fourth generation axion helioscope based on improving the magnetic field volume, X-ray focusing optics and detector technology of the current state-of-the-art helioscope, the CERN Axion Solar Telescope (CAST) [6,7] that started operating in 2003 and finished its data taking in 2021 at the European Organization for Nuclear Research (CERN). IAXO is planned to be installed at DESY (Deutsches Elektronen-Synchrotron) in Hamburg, Germany, and plans to search for solar axions through the inverse Primakoff effect [8].

Axions are candidates to dark matter [9] and can also be produced in the solar interior [10,11], and the solar axion emission rate produced by the usual Primakoff effect can be calculated from the spectrum of $\mathbf{E}\cdot\mathbf{B}$ fluctuations, where $\mathbf{E}$ comes from the charged particles forming the plasma and $\mathbf{B}$ is generated by the propagation of thermal photons [12]. The Primakoff solar axion flux spectrum can be expressed analytically as

$$\frac{\mathrm{d}\phi_a}{\mathrm{d}E} = 6.02 \cdot 10^{10} g_{10}^2 E^{2.481} e^{-E/1.205} \mathrm{cm}^{-2}\mathrm{s}^{-1}\mathrm{keV}^{-1}, \quad (1)$$

where $g_{10} = 10^{-10}\,\mathrm{GeV}^{-1}$ and E is the axion energy in keV.[1]

* Corresponding author at: Institute of Experimental Physics. University of Hamburg, Luruper Chaussee 149 22761, Hamburg, Germany.
** Corresponding author.
*** Corresponding author at: Fakultät für Physik. Technische Universität Dortmund., Dortmund, D-44221, Germany.
E-mail addresses: itxaso.antolin.rojo@uni-hamburg.de (I. Antolín), 821199@unizar.es (A. Huerva), Jaime.Ruz@tu-dortmund.de (J. Ruz).

[1] A more physically motivated fit has been proposed in [13], where the parameters possess direct physical interpretations, like average energy E_0 and a β index indicating how close to thermal the spectrum is.

https://doi.org/10.1016/j.nima.2026.171585
Received 13 November 2025; Received in revised form 20 March 2026; Accepted 13 April 2026
Available online 16 April 2026

There also exist other solar hadronic axion emission mechanisms independent from the axion–photon coupling. Such is the case of the magnetic dipole (M1) nuclear transition of ^{57}Fe at 14.4 keV.[2] The flux of the monoenergetic solar axions produced via this process was computed in [14,15]:

$$\Phi_a = 4.56 \times 10^{23} \left(g_{aN}^{eff}\right)^2 \ \mathrm{cm}^{-2}\mathrm{s}^{-1}, \tag{2}$$

where $g_{aN}^{eff} = (-1.19\, g_{aN}^0 + g_{aN}^3)$ is considered a free unknown parameter that characterizes the axion–nucleon coupling[3] [14,15]. Apart from hadronic axion models, there are other mechanisms for axion emission from the Sun. For instance, the non-hadronic models, which allow for axion–electron coupling at tree-level via g_{ae}, leading to larger axion fluxes from stars than the traditionally studied Primakoff emission [16,17]. See [13] for accurate quasi-thermal descriptions of Bremsstrahlung and Compton processes. In the following, we refer to the non-hadronic flux as BCA, denoting the combined contributions from bremsstrahlung, Compton scattering, and atomic recombination. A summary of the relevant Feynman diagrams is shown in Fig. 1.

The International Axion Observatory is a next-generation axion helioscope designed to search for solar axions and axion-like particles through their conversion into X-ray photons in a strong transverse magnetic field. Building upon the experience gained with the CERN Axion Solar Telescope, IAXO will employ a purpose-built superconducting toroidal magnet with several parallel bores, each equipped with grazing-incidence X-ray optics that focus the converted photons onto ultra-low-background detectors. The experiment aims to improve the sensitivity to the axion–photon coupling constant, $g_{a\gamma}$, by more than an order of magnitude beyond CAST [18]. Notably, it may become the first experiment capable of probing regions of parameter space where the sensitivity exceeds existing astrophysical constraints on the axion–electron coupling, g_{ae}. Furthermore, with an appropriately optimized detector configuration, IAXO has the potential to achieve sensitivity to axion–nucleon couplings, g_{aN} [19]. As an intermediate step toward the full experiment, BabyIAXO [20] is being developed as a prototype helioscope that will validate the key technologies of IAXO, including the magnet design, X-ray optics, solar tracking system, and low-background detector technologies such as Micromegas. In addition to serving as a technological demonstrator, BabyIAXO will already provide competitive physics reach and enable the exploration of new regions of axion and axion-like particle parameter space. See Fig. 2 for an engineering view of the proposed BabyIAXO setup at DESY.

This paper investigates the performance of the IAXO Micromegas detectors and examines the influence of alternative gas mixtures and extended drift geometries on enhancing sensitivity to various axion couplings, with particular emphasis on the axion–nucleon interaction channel. Using detailed simulations, we evaluate the intrinsic detection efficiency across multiple detector configurations and estimate the corresponding signal-to-noise ratios while accounting for cosmic-ray-induced background contributions. The results establish a comparative framework for optimizing detector design parameters in future axion search experiments.

2. IAXO micromegas detectors

IAXO incorporates gaseous low-background, pixelated X-ray detectors positioned at the focal planes of its X-ray optics. These detectors utilize advanced Time Projection Chamber (TPC) technology, featuring compact chambers with 6 cm diameter and 3 cm drift distance. The

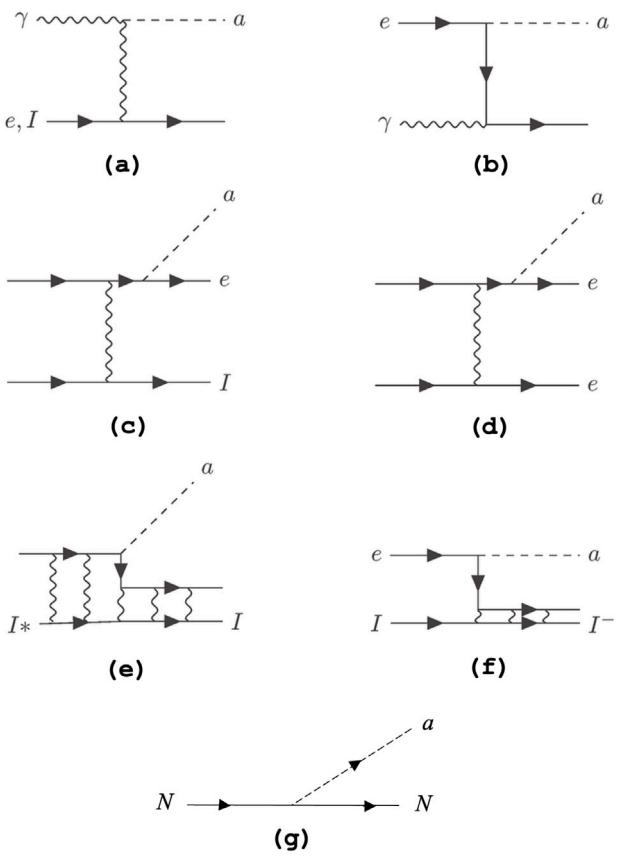

Fig. 1. Feynamn diagrams for (a) Primakoff, (b) Compton, (c) $e^- I$ bremsstrahlung, (d) $e^- e^-$ bremsstrahlung, (e) axio-deexcitation, (f) axiorecombination and (g) axion–Nucleon couplings.

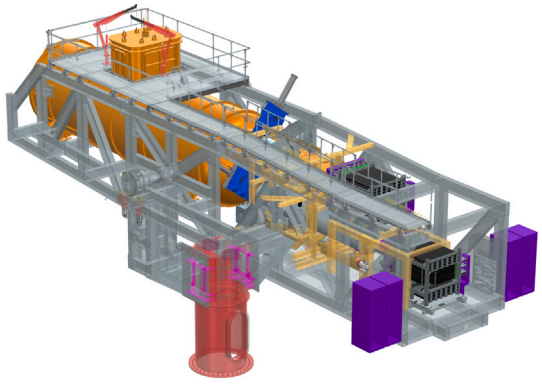

Fig. 2. Schematic representation of the BabyIAXO experimental setup. The magnet vessel (orange) houses the 10 m long superconducting magnet with two 700 mm diameter bores. The detector systems (black) are positioned at the end of the beamline and are surrounded by passive shielding and active muon veto detectors for background suppression. In purple, electronic racks for detector electronics and other services. DN800 gate valves (blue) provide vacuum isolation between the magnet vessel and the beamline. Inside the beamline, close to the gate valve, X-ray telescopes are installed and operated under vacuum to focus the expected axion-to-photon conversion signal onto the detectors. The entire magnet–beamline assembly is supported by a mechanical platform (light gray), while a pivoting tracking platform (red) allows the instrument to follow the Sun during data-taking.

[2] Magnetic dipole transition between the first excited state ($I^\pi = 3/2^-$) and the ground state ($I^\pi = 1/2^-$). This transition is the basis of the Mössbauer effect in ^{57}Fe and is widely used as a narrow and well-defined γ-ray reference line in nuclear spectroscopy.

[3] It may be helpful to clarify that these correspond to the isoscalar and isovector axion–nucleon couplings, respectively. The relations $g_{an} = g_{aN}^0 - g_{aN}^3$ and $g_{ap} = g_{aN}^0 + g_{aN}^3$ then connect this notation to the usual neutron and proton couplings.

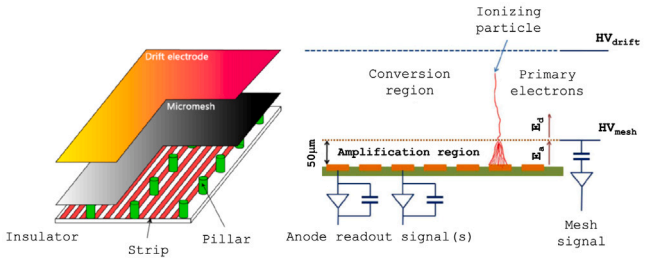

Fig. 3. Micromegas detector layout showing the drift region, amplification gap, micromesh, and readout plane. Fig.adapted with permission from [22].

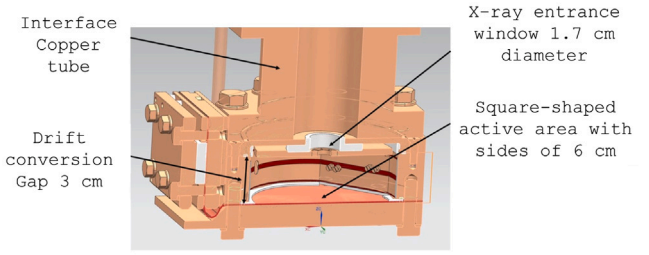

Fig. 4. IAXO-D1 detector prototype design showing the 3 cm drift region separated by an X-ray transparent window from the copper tube that connects to the optics. The readout plane or anode is seen at the bottom of the chamber [20].

readout system employs micro-mesh gaseous structure (Micromegas) technology, fabricated using the microbulk technique [21]. In the IAXO-D1 prototype studied here, the amplification stage consists of two parallel electrodes separated by a 50 μm gap (see Fig. 3) and it is defined by a fine copper micro-mesh (5 μm thick), while the readout plane is formed by copper strips, and the pixelated readout structure is defined by the intersections of orthogonal strip layers. Ionization events within the gaseous medium release electrons that drift toward the mesh before entering the amplification gap along the electric field lines. The readout area of the detector spans 60 × 60 mm^2, incorporating 120 strips per axis with a 500 μm pitch and the selected avalanche gap ensures for efficient charge amplification and signal detection [22].

The standard operational setup of the detector makes use of argon gas at 1.2 bar pressure, supplemented with 1% isobutane (C_4H_{10}) as a quencher. The potential X-rays from axion-to-photon conversion coming from IAXO's magnet enter the Micromegas conversion volume through a window made of ∼ 4 μm aluminized Mylar foil, which serves as the TPC cathode. This window is reinforced by a metallic strong-back to withstand the pressure difference relative to the magnet vacuum (or buffer gas) system [20]. The TPC body and chamber walls are constructed from 18 mm thick radio-pure oxygen-free copper and are connected to the conversion magnet via a copper interface tube of the same characteristics and thickness. It also has a field shaper to enhance the uniformity of the drift field and minimize border effects. The detector chamber was manufactured at the University of Zaragoza, Spain, while the readout plane — realized on a flexible Kapton substrate using the microbulk Micromegas technique — was fabricated at the laboratory of Rui de Oliveira at CERN, a facility renowned for its advance manufacturing methods in Micromegas technology [21]. This process, coordinated with CEA/IRFU, ensures precise patterning and uniformity across the detector, providing the mechanical and electrical stability required for high-resolution particle tracking and low-background X-ray detection [23].

The topological characteristics of events recorded by the Micromegas readout plane allow for clear discrimination between genuine X-ray signals and background interactions within the drift chamber. Signal

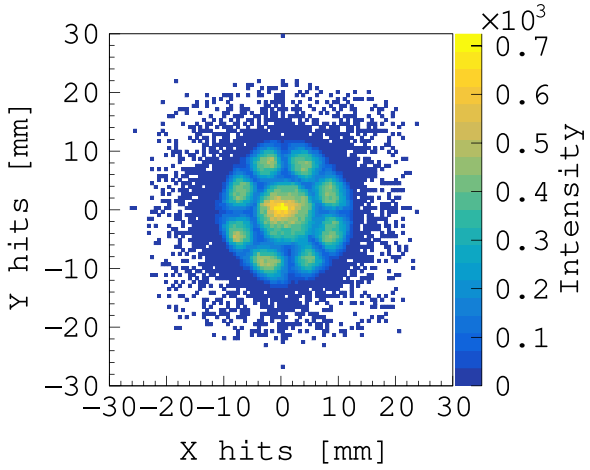

Fig. 5. Hit map (scatter plot) of an ^{55}Fe calibration for the IAXO-D1 prototype, showing the spatial distribution of X-ray interactions across the detector's active area, with the color scale indicating event intensity.

events, such as those produced by X-rays from axion-to-photon conversion or calibration sources, typically produce compact, localized clusters of hits confined to a few readout strips or pixels. In contrast, background events originating from cosmic rays, environmental gamma radiation, or alpha particles often exhibit extended or irregular hit patterns, with multiple clusters, elongated tracks, or higher multiplicity across the readout plane. These differences in topology can be exploited to implement software-based background rejection, enhancing the signal-to-noise ratio. The fundamental design of the detector prototype, IAXO-D1, is illustrated in Fig. 4, and is presently undergoing characterization by the IAXO Collaboration. Fig. 5 illustrates a typical hit map obtained during calibration of the IAXO-D1 detector using a^{55}Fe source, where the compact clusters corresponding to X-ray interactions are clearly visible.

To minimize background contributions, the detector components are selected from highly radio-pure materials and are encased within both passive and active shielding. Passive shielding consists of 20 cm lead and the already mentioned 18 mm copper, while active shielding employs 10 cm thick muon vetoes using BC 408[4] scintillating plastics to mitigate muon cosmic radiation effects. Together, and by means of event discrimination strategies that analyze the topological properties of background events, the Micromegas detectors of IAXO are able to achieve a background level of 8.6×10^{-7} counts keV^{-1} cm^{-2} s^{-1}, with an energy threshold of ∼ 1 keV [24].

2.1. Intrinsic efficiency of IAXO-D1

A novel computational code [25] has been developed to evaluate the efficiency of the detector at specific energies. To achieve this, simulations were conducted using RestG4, a REST-for-Physics-based framework [26] (v.2.4.3) that integrates the Geant4 [27] library (v.11.0.3) to define boundary conditions, execute simulations, and collect results in the form of ROOT files encapsulated as REST C++ objects. The geometry of the IAXO-D1 detector was implemented in accordance with the guidelines provided in IAXO's official repository [28]. For extended drift configurations with a distance of 6 cm, the original design was modified accordingly. This extension is motivated by the attenuation length of X-rays in the drift gas, which depends on both

[4] BC-408 is a polyvinyltoluene-based plastic scintillator commonly used for muon detection. It is a fast-response scintillator produced by Saint-Gobain and widely employed in particle physics experiments due to its high light output and short decay time.

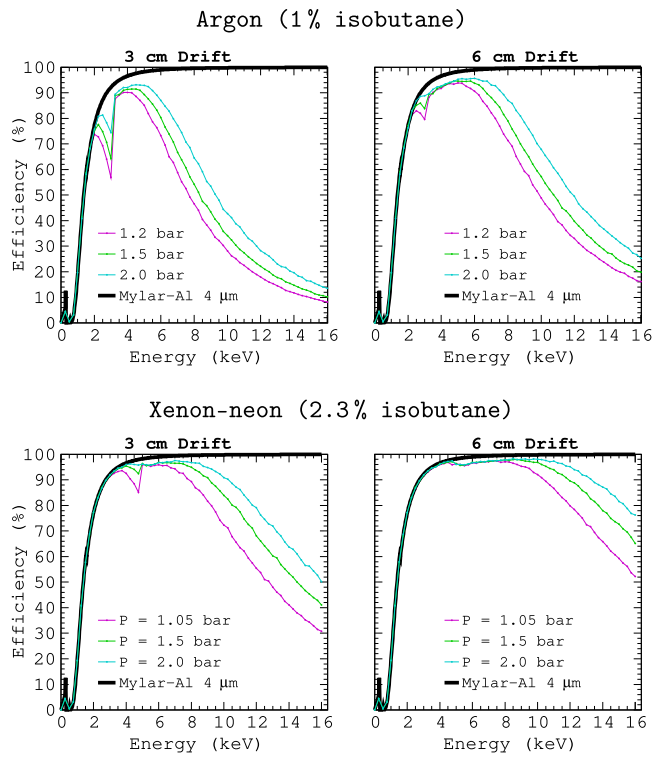

Fig. 6. Intrinsic efficiency of IAXO-D1 for argon (top) and Xe-Ne (bottom). Study performed for both, a 3 cm drift (left) and a 6 cm drift (right). Photon transmission across the aluminized Mylar window is shown in black.

the photon energy and the specific gas mixture used in the drift volume. For example, in argon-based mixtures, a drift length of about 3 cm is typically sufficient for X-rays below approximately 6 keV due to their relatively short attenuation length. At higher photon energies, however, the photoelectric absorption cross-section decreases and photons travel longer distances before interacting, requiring a larger drift volume to maintain good detection efficiency. In addition, for photon energies above the argon K-shell binding energy,[5] the interaction may produce characteristic argon fluorescence X-rays that can escape the active volume, leading to the appearance of an argon escape peak in the measured spectrum. Increasing the drift distance therefore improves the probability that the primary photon energy is fully absorbed within the detector. The choice of a 6 cm drift length represents a compromise: significantly longer drift regions would require more complex field-shaping ring configurations to maintain a uniform electric field, while the background registered by a TPC detector generally increases proportionally with the gas volume in the drift chamber.

To determine the intrinsic efficiency of IAXO-D1, mono-energetic X-ray events within the energy range of 0–16 keV were generated at 0.25 keV intervals in front of the Mylar window under vacuum conditions. Each simulation was configured to record 10,000 events within the detector, ensuring a consistent statistical uncertainty across all energy values. The detector volume was filled with either an Ar + 1% C_4H_{10} gas mixture or a purpose made gas blend of 48.85% xenon, 48.85% neon and 2.3% isobutane, and the simulation data were stored in ROOT files. A conservative approach was adopted for efficiency calculations: an event was only considered valid if it produced an energy deposition (or hit) in the sensitive volume equal to the initial X-ray energy; otherwise, it was not considered.

[5] Argon: $K_{\alpha_1} = 2957.7$ eV; $K_{\alpha_2} = 2955.63$ eV; $K_{\beta_1} = 3190.5$ eV [29].

The simulation results are presented in Fig. 6, illustrating efficiency curves for various argon pressure values: 1.2 bar, a typical configuration for data acquisition; 1.5 bar; and 2.0 bar, the maximum pressure difference tolerated by the current Mylar window design. These simulations assess detector performance at higher gas densities for the Ar-isobutane mixture. Additionally, the Xe-Ne mixture was studied at pressures of 1.05 bar, 1.5 bar, and 2.0 bar. The choice of 1.05 bar is deliberate, matching the operating pressure of the xenon-based prototype detector employed in CAST [7] and during the initial sea-level characterization of IAXO-D1 at the University of Zaragoza [24].

Fig. 6 demonstrates that, for argon, detector efficiency improves with both an increased chamber size and higher pressure, particularly for energies above 4 keV. Notably, the argon escape peak, which appears around 3 keV, becomes nearly negligible at 2.0 bar. Interestingly, the proposed Xe-Ne mixture with a 3 cm drift chamber already outperforms the efficiency achieved by a 6 cm drift chamber filled with Ar-isobutane. This effect becomes particularly significant at energies above 8 keV, underscoring a viable strategy for enhancing the axion–nucleon sensitivity of the IAXO experiment. Furthermore, Fig. 6 suggests that the 4 µm aluminized Mylar window plays a defining role in determining the energy threshold of the IAXO-D1 prototype. The choice of a thin Mylar window supported by a strongback structure is driven by mechanical and operational requirements. In particular, the window must withstand the differential pressure between the magnet bore, that it is kept under high vacuum to allow the efficient propagation of photons produced via axion-to-photon conversion, and the drift region of the detector, which is filled with photon-detection gas mixtures at pressures at or above atmospheric levels. The strongback provides the necessary mechanical support to maintain the structural integrity of the thin membrane under this pressure difference while preserving a high photon transmission. The aluminum layer on top of the Mylar membrane serves two purposes. First, it provides a conductive surface that can be biased at high voltage, allowing the window to function as the cathode of the TPC. Second, the aluminum coating reduces the gas permeability of the Mylar by sealing microscopic pores in the material, thereby limiting gas transmission through the membrane. This helps preserve the vacuum quality in the axion-to-photon conversion region while maintaining stable pressure conditions within the detector drift volume. Alternative window technologies will also be explored in future setups. In particular, ultra-thin SiNx windows could significantly improve the X-ray transmission in the low-energy region of interest (0–3 keV) [30]. However, these solutions currently present important technological challenges, mainly because their mechanical robustness typically requires smaller window diameters than those compatible with the relatively large active area of the present Micromegas readout plane. Achieving a sufficiently large and stable window capable of withstanding the required differential pressure while maintaining high transmission therefore remains an active area of development.

3. Geant4 simulations for axion discovery

This section examines the three distinct solar axion spectra arising from axion–photon, axion–electron, and axion–nucleon couplings, in contrast to the mono-energetic simulations presented in the previous chapter. The discussion is structured into two subsections: the first focuses on simulating the energy depositions associated with the three raw spectra, while the second applies diffusion and attachment effects intrinsic to TPC-Micromegas detectors.

3.1. Nominal photon flux at the detector

The nominal photon flux for each spectrum is defined using ROOT::TH1D histograms, which provide RestG4 with the probability distribution of incoming photons to the IAXO-D1 prototype. Simulations have been performed for argon-isobutane gas mixtures at

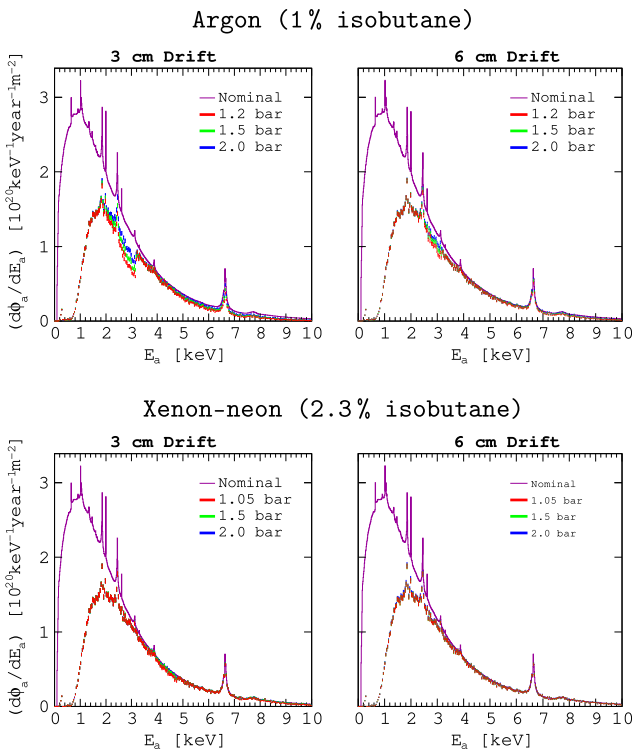

Fig. 7. Detected BCA flux with argon (top) and Xe-Ne (bottom). Study performed for both, a 3 cm drift (left) and a 6 cm drift (right).

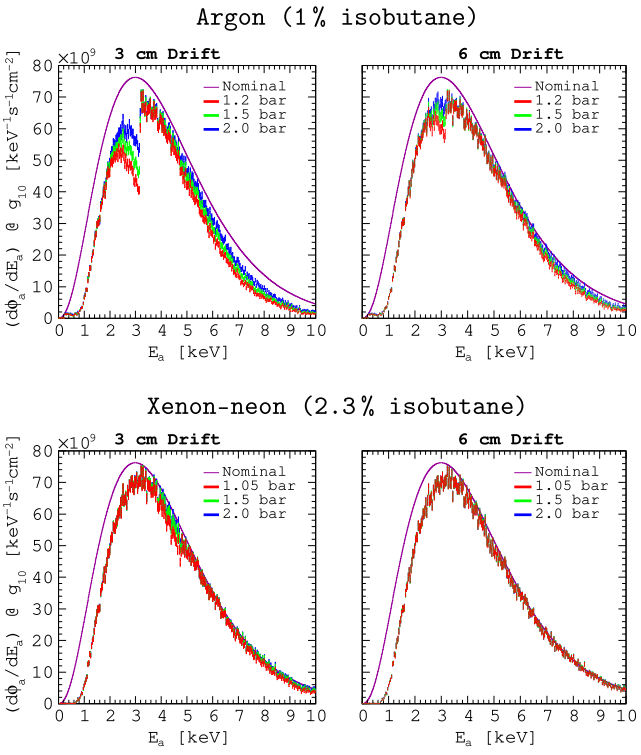

Fig. 8. Detected Primakoff flux with argon (top) and Xe-Ne (bottom). Study performed for both, a 3 cm drift (left) and a 6 cm drift (right).

pressures of 1.2, 1.5, and 2.0 bar, considering both the IAXO-D1 prototype and an extended geometry of 6 cm. Equivalent simulations have

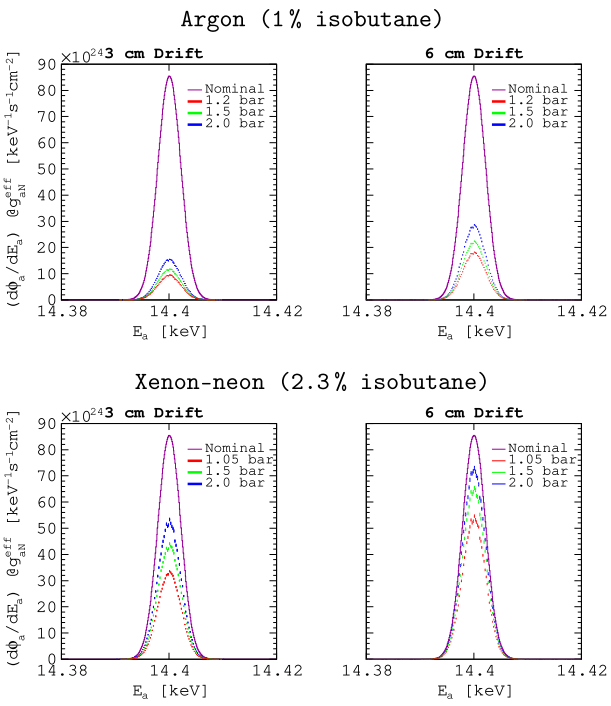

Fig. 9. Detected axion–nucleon flux with argon (top) and Xe-Ne (bottom). Study performed for both, a 3 cm drift (left) and a 6 cm drift (right).

been conducted for the proposed Xe-Ne mixture at pressures of 1.05, 1.5, and 2.0 bar. Statistical uncertainties have been incorporated based on the Poisson distribution [31]. The number of recorded events is set to 200,000 for the BCA, Primakoff and for the axion–nucleon fluxes.

The results for the BCA photon flux are presented in Fig. 7, while those for the Primakoff photon flux are shown in Fig. 8. Simulations of the axion–nucleon photon flux, which peaks at approximately 14.4 keV, are depicted in Fig. 9. As expected, increasing the detector's operating pressure or doubling the nominal drift distance of the IAXO-D1 prototype significantly enhances detection efficiency. Notably, however, the use of a Xe-Ne mixture surpasses these optimization strategies, particularly at higher energies. This effect is most pronounced in the case of axion–nucleon coupling, where the Xe-Ne mixture clearly outperforms argon-based mixtures.

3.2. Study of the detector response

To further refine our study, the spectra obtained in the previous subsection have been analyzed using the REST software to account for the detector's energy resolution and the diffusion process.

The first step of the analysis involves extracting information on energy depositions generated by primary events from the Geant4 Monte Carlo simulations presented in the preceding section. The electromagnetic interactions and physical processes considered, introduced at the beginning of this section, are designed to accurately reproduce the detector's energy resolution, as measured during the laboratory characterization of the IAXO-D1 prototype. Specifically, the analysis applies a stochastic smearing process [32] to the energy of detected hits, redistributing the total energy of each event according to a Gaussian function.

The smearing process is based on experimental calibrations of the IAXO-D1 prototype using ^{55}Fe [24]. To incorporate the energy dependence of the detector's resolution, a theoretical scaling relation is applied: $R(E) = R(E_{ref}) \times \sqrt{E_{ref}/E}$, where E_{ref} denotes the centroid energy of the ^{55}Fe calibration line, and $R(E_{ref})$ represents the measured energy resolution at this reference point. For simplicity, it is

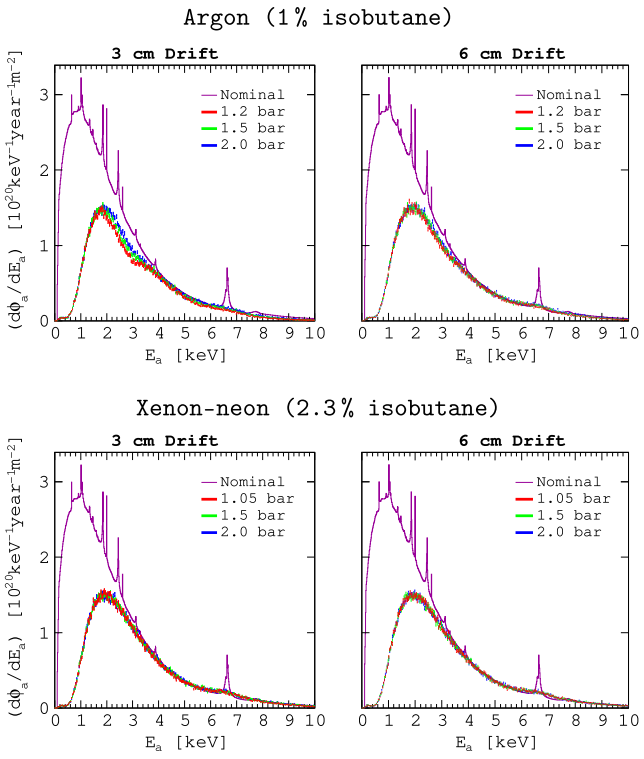

Fig. 10. IAXO-D1 detected solar BCA axion flux with argon (top) and Xe-Ne (bottom). Study performed for both, a 3 cm drift (left) and a 6 cm drift (right).

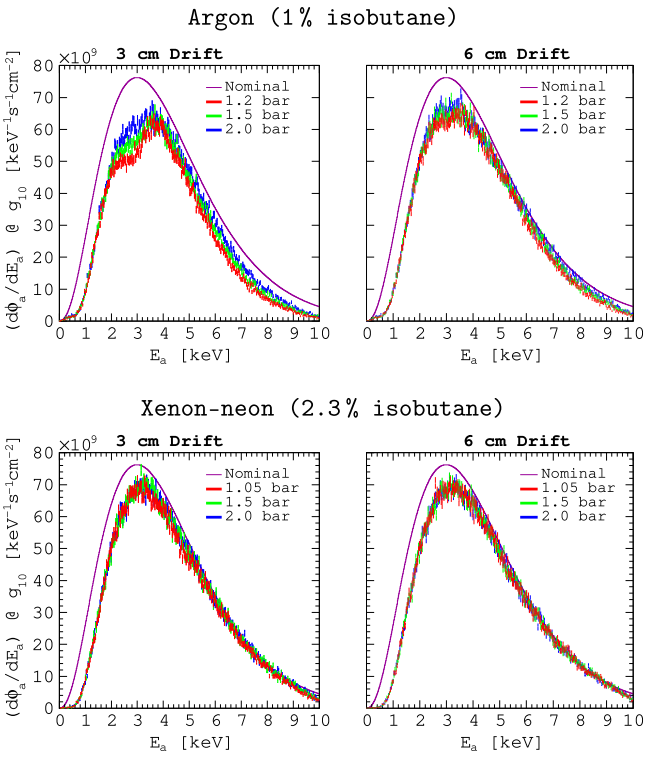

Fig. 11. IAXO-D1 detected Primakoff solar axion flux with argon (top) and Xe-Ne (bottom). Study performed for both, a 3 cm drift (left) and a 6 cm drift (right).

assumed that the detector's energy resolution remains consistent across both chamber sizes. A third analysis has been conducted to model electron diffusion in the gaseous medium. This process makes use of *Magboltz* [33] to compute the transport properties of electrons in the gas mixture via the *Garfield* toolkit [34], which is integrated into REST. The simulation employs the longitudinal and transverse diffusion coefficients of the different gas mixtures to replicate the relative displacement of electrons from their original positions, attributed to primary ionization [35]. In this approach, the energy of each hit is converted into the corresponding number of primary electrons generated in the ionization process, as it is directly related to the deposited energy through the material's work function (W-value). Each electron is then treated as an individual hit, and its spatial coordinates are randomly displaced according to a Gaussian distribution, determined by the gas parameters, longitudinal and transverse diffusion coefficients, and the distance to the readout plane.

To achieve this, the gas mixtures, pressure, and an electric drift field of 145 V cm^{-1} are considered. This electric field has been selected for a 3 cm drift distance, assuming a cathode voltage of 750 V and a mesh voltage of 315 V —conservative values consistent with previous data acquisitions [24]. This configuration is maintained for the extended 6 cm drift chamber, which would require a cathode voltage of 1500 V to keep the same field strength.

4. Performance

This section presents the analyzed spectra obtained in the previous Section 3.1 after including IAXO-D1 detector response. Photon fluxes resulting from axion–electron coupling are shown in Fig. 10 and are consistent with the simulated spectra in Fig. 7. Notably, the smearing and diffusion processes introduce significant blurring, leading to the complete disappearance of the characteristic peaks in the BCA flux. This effect was anticipated due to the energy resolution of the IAXO-D1 prototype for both gas mixtures. However, the proposed Xe-Ne mixture does not demonstrate a clear advantage over the conventional argon-isobutane setup. This is primarily because, apart from the argon escape peak, the standard Micromegas configuration remains highly efficient at energies below 6 keV.

Similar conclusions can be drawn from the analysis of the Primakoff spectra presented in Fig. 11, which follow the simulated spectra shown in Fig. 8. As in the previous case, hit events are redistributed according to the detector's response characteristics. Notably, the argon escape peak is visible only in the 3 cm chamber configuration, with increasing efficiency observed at higher argon gas pressures. However, for the solar axion flux originating from Primakoff conversion, Xe-Ne mixtures exhibit comparable performance even at low gas pressure and within a 3 cm drift chamber.

To finalize, the axion–nucleon spectra obtained from this analysis are presented in Fig. 12. For clarity, the nominal axion–nucleon spectrum has been omitted, as the detected flux in the analyzed data is significantly lower than that observed with the IAXO-D1 prototype. This reduction is attributed to the detector's efficiency and energy resolution, which causes the counts to be distributed over a broader Gaussian profile compared to the M1 ^{57}Fe transition line originating from the Sun. Additionally, Fig. 12 highlights secondary excitations occurring within the detector. Considering that the primary k-emission of argon is approximately 3 keV [29], a straightforward calculation confirms that the peak observed around 11.5 keV corresponds to the argon escape peak associated with the expected M1 ^{57}Fe transition. Furthermore, the peak at approximately 8 keV is identified as the copper fluorescence line [29] arising from the detector passive shielding setup. The copper fluorescence is also present for the Xe-Ne setup, but in this case, there is no escape peak associated, since the nature of the gas is different. Note that the k-alpha fluorescence of xenon is at 29.5 keV and neon has a low fluorescence yield (< 5%) for k-shell transitions.

In the case of axion–nucleon interactions, the proposed Xe-Ne mixture demonstrates superior performance compared to argon gas, regardless of the drift configuration considered. Notably, a 3 cm drift

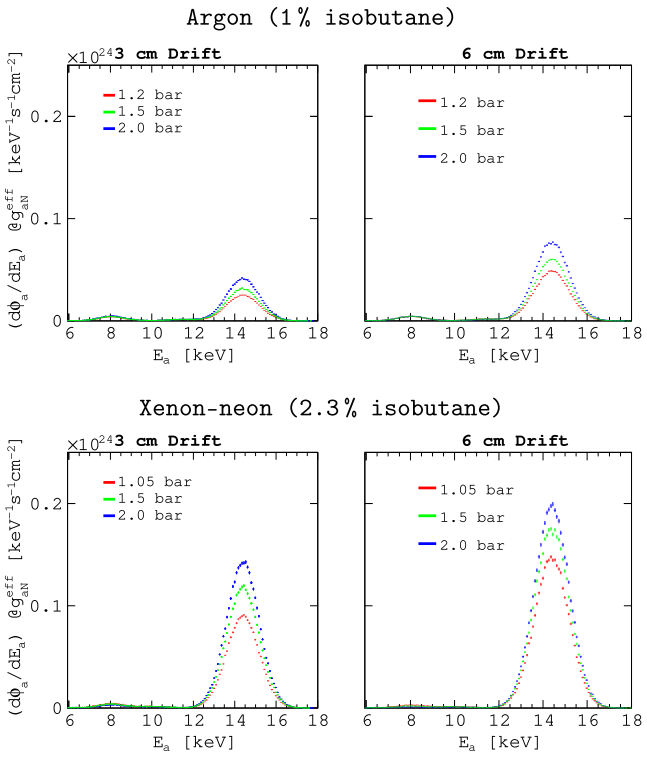

Fig. 12. IAXO-D1 detected solar axion–nucleon flux with argon (top) and Xe-Ne (bottom). Study performed for both, a 3 cm drift (left) and a 6 cm drift (right).

Table 1
Comparison of integrated efficiency using different mixtures and pressures for a 3 cm drift chamber (top) and for a 6 cm drift distance (bottom).

	3 cm drift distance chamber			
	$P_{(bar)}$	$BCA_{(\%)}$	$Primakoff_{(\%)}$	$aN_{(\%)}$
Argon	1.2	49.34 (0.14)	71.15 (0.21)	10.87 (0.03)
	1.5	51.45 (0.14)	75.15 (0.22)	13.55 (0.03)
	2.0	53.66 (0.15)	79.41 (0.24)	17.87 (0.04)
Xe-Ne	1.05	56.41 (0.16)	84.78 (0.26)	38.83 (0.10)
	1.5	57.04 (0.16)	86.43 (0.26)	50.81 (0.14)
	2.0	57.25 (0.16)	86.97 (0.27)	61.35 (0.18)
	6 cm drift distance chamber			
	$P_{(bar)}$	$BCA_{(\%)}$	$Primakoff_{(\%)}$	$aN_{(\%)}$
Argon	1.2	54.57 (0.15)	81.05 (0.25)	21.07 (0.05)
	1.5	55.58 (0.16)	83.14 (0.25)	25.79 (0.07)
	2.0	56.44 (0.16)	85.03 (0.26)	33.08 (0.09)
Xe-Ne	1.05	57.24 (0.16)	86.95 (0.27)	63.12 (0.18)
	1.5	57.35 (0.16)	87.20 (0.27)	75.90 (0.23)
	2.0	57.99 (0.16)	87.22 (0.27)	84.92 (0.26)

chamber operating with Xe-Ne at 1.5 bar is twice as efficient than a 6 cm drift chamber filled with argon gas at the same pressure. See Table 1, where the overall efficiencies have been calculated integrating from 0-to-10 keV in the case of axion-Primakoff and BCA models, and from 12-to-17 keV for axion–nucleon searches. The percentages reported in Table 1 represent the fraction of flux capable of producing signals in the different setups of the IAXO-D1 detector drift regions relative to the total flux present in the magnetic conversion region of the experiment.

4.1. Sensitivity studies

The sensitivity to the axion couplings $g_{a\gamma}$, g_{ae} and g_{aN} not only depends on N_γ, the expected photons arriving to the detector from axion conversions (i.e. the detector efficiency), but also on the background counts of the experiment, N_b. In the general case where the measurement is dominated by background events ($N_b > N_\gamma$), and the relevant coupling constant is $g_{a\gamma}$, the discovery potential of the experiment scales with the signal-to-noise ratio, approximately as $N_\gamma/\sqrt{N_b}$.

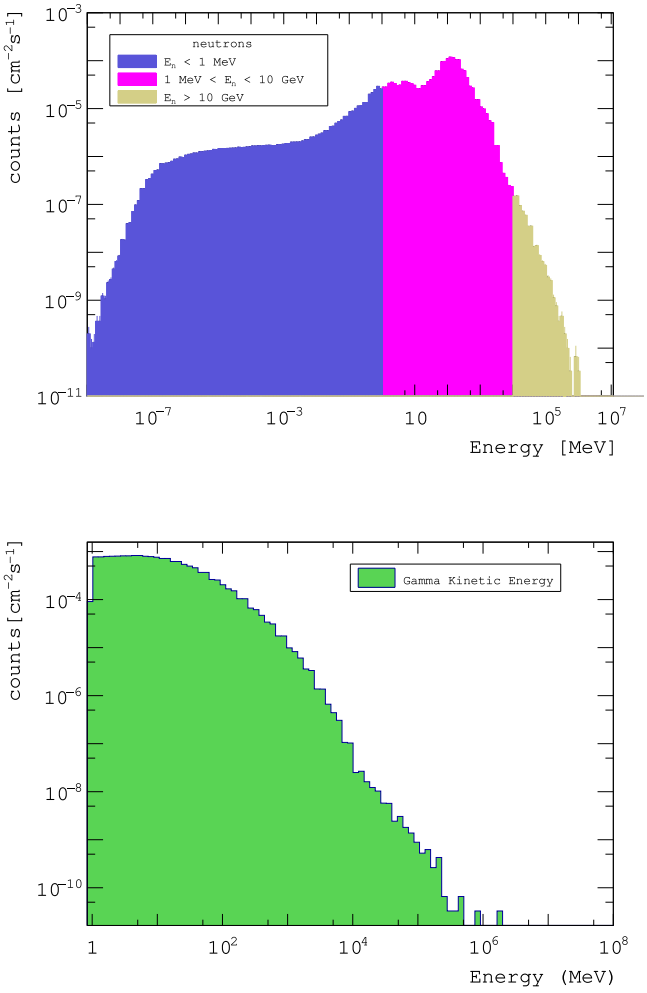

Fig. 13. Energy distribution of cosmic-induced neutrons (top) and gammas (bottom) at sea level [36].

Since IAXO and its precursor BabyIAXO are designed to operate at sea level, cosmic-ray-induced radiation is expected to constitute the dominant background contribution. In particular, secondary neutrons and gamma rays produced by interactions of primary cosmic protons in the atmosphere represent the main sources of energy deposition in the Micromegas drift region. To quantify these effects, detailed Monte Carlo simulations have been performed using the Geant4 toolkit in combination with the REST-for-Physics framework. The employed cosmic-ray generator models the production and transport of secondary particles — including neutrons, muons, gamma rays, electrons, and pions — originating from primary protons in the energy range from 1 GeV to 100 TeV [36].

Background contributions from radon are effectively mitigated by enclosing the detector and its passive shielding within a pressurized nitrogen atmosphere, which suppresses the contribution of radon progeny into the active volume. Under these conditions, cosmic radiation remains the primary limiting factor for detector sensitivity. The IAXO design inherits and further develops the background reduction strategies established in CAST, including those implemented in its TPC [37,38] and Micromegas detectors [39,40].

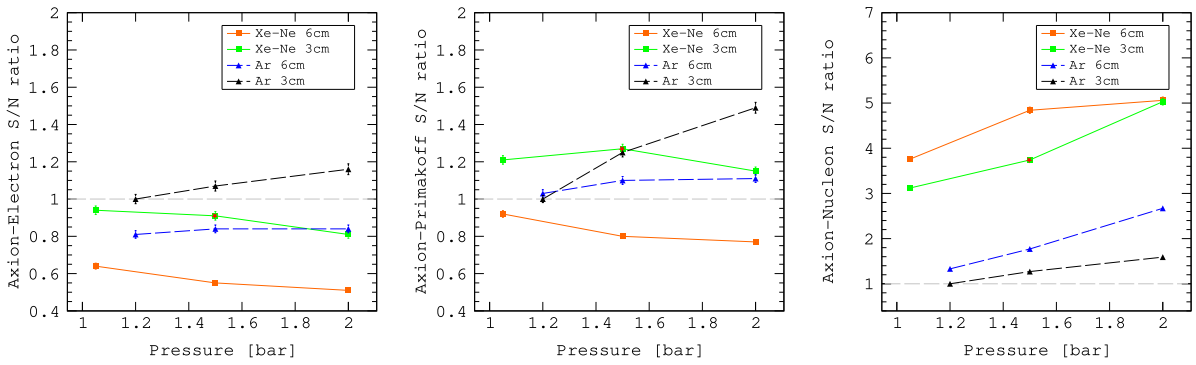

Fig. 14. IAXO-D1 signal-to-noise ratio for BCA (left), Primakoff (middle), and axion–nucleon (right) couplings. The signal-to-noise ratios are shown relative to the argon baseline detector configuration (1.2 bar pressure and a 3 cm drift chamber), indicated by the dashed gray horizontal line in each panel. A red star marks a potentially favored configuration: a Xe–Ne gas mixture at 1.5 bar pressure. This setup increases the S/N ratio by 27% for the Primakoff flux and by a factor of 3.6 for the axion–nucleon flux, while keeping the BCA S/N ratio consistent with the baseline within the statistical uncertainties of our simulations.

The present cosmic background model incorporates neutron and gamma-ray spectra (see Fig. 13), while the contribution from muons is not explicitly simulated due to the high efficiency of the surrounding veto system [24]. A conservative approach is adopted, assuming total detection efficiency for background events within the active volume, whereas topological discrimination is included only in the signal efficiency. Surface contamination is assumed to be independent of the gas configuration, and residual radon-induced contributions are considered negligible.

The IAXO-D1 detector has been specifically designed to minimize background levels. All components are fabricated from ultra-radiopure materials, screened at the Canfranc Underground Laboratory using low-background germanium detectors [41]. The detector is enclosed within an integrated shielding system combining passive and active elements. The passive shielding consists of a multilayer structure of copper and lead (described in Section 2), while the active shielding is provided by a 4π plastic scintillator muon veto system. Additional background suppression is achieved through event-topology-based discrimination techniques in the Micromegas detector [24].

Radiogenic backgrounds from detector materials and environmental radioactivity (e.g. the decay chains of ^{238}U, ^{232}Th, and ^{40}K) are not included in this study. The goal is to isolate the contribution of cosmic-ray-induced backgrounds and enable a relative comparison of detector configurations. Accordingly, this work does not aim to provide a complete and fully realistic background model — an inherently complex and ongoing effort [24,40,42] — but rather to identify robust trends as a function of gas pressure and detector volume under simplified, conservative assumptions. A comprehensive model, incorporating radiogenic contributions and informed by dedicated environmental measurements at the experimental site, will be developed in future studies.

To assess the relative performance of the detector configurations considered in this work, the corresponding axion signal-to-noise ratios are evaluated, taking as reference a standard argon–isobutane gas mixture at 1.2 bar. For each configuration, 12,000 events are simulated in order to reduce statistical uncertainties. The results, shown in Fig. 14, combine the integrated detection efficiency with the simulated cosmic-ray-induced background for the IAXO-D1 detector. The assumed shielding configuration consists of 18 mm of copper, 20 cm of lead, and 10 cm of muon veto material, fully enclosing the detector volume.

As shown in Table 1, one might initially consider increasing the drift distance of IAXO-D1 from 3 cm to 6 cm to enhance the detector's sensitivity to axion–nucleon couplings. This modification could potentially improve the experiment's reach while maintaining, or even enhancing, its detection efficiency for axions produced through the Primakoff and BCA channels. The Primakoff channel is particularly crucial because it is present in all axion models and its production mechanism is guarantied in the solar core via the conversion of thermal photons. Moreover, it coincides with the detection process exploited in IAXO, where solar axions can reconvert into photons in a strong laboratory magnetic field. This unique feature provides a direct and highly controlled pathway to study $g_{a\gamma}$, making the Primakoff channel the primary discovery channel for helioscopes and haloscopes [43]. In the BCA scenario, IAXO's sensitivity depends on the product of the axion–electron and axion–photon coupling constants, leading to exclusion limits in the $g_{a\gamma}-g_{ae}$ parameter space. A similar approach applies to axion–nucleon couplings, for which results are presented in the $g_{a\gamma}-g_{aN}$ parameter space. Optimizing the detector to efficiently capture both fluxes ensures that IAXO-D1 can explore multiple discovery channels simultaneously, maximizing its potential to detect or constrain a broad range of axion properties (see Ref. [18] for a detailed discussion of these channels and their significance). As expected, and as it is shown in Fig. 14, simulations of cosmic-induced background for the considered detector shielding, gas mixtures, and drift geometries indicate that increasing the drift distance also raises the background level observed by the Micromegas detectors, reducing the overall benefit. Instead, the custom Xe–Ne mixture proposed in this work, operated at pressures between 1 and 1.5 bar with a 3 cm drift region, yields a factor of 3.1–3.7 improvement in sensitivity to axion–nucleon couplings compared with the conventional 1.2 bar Ar-based configuration. This improvement is achieved while largely preserving the sensitivity to axion–Primakoff and axion–electron signals, with a signal-to-noise gain of 21%–27% for the Primakoff channel and a modest 6%–9% reduction for axion–electron couplings at 1 and 1.5 bar, respectively. The energy ranges considered for the axion–electron, axion–Primakoff, and axion–nucleon searches are 0.5–4 keV, 2–7 keV, and 12–17 keV, respectively.

Table 2 summarizes the statistical results of the simulated cosmic-ray-induced events for the different Micromegas configurations. For each gas mixture and pressure, the table reports the number of generated primary particles (neutrons and gammas). The relative contributions of neutron- and gamma-induced interactions are listed separately, together with the total number of registered events in the Micromegas detector and their statistical uncertainties.

The resulting background levels, signal efficiencies, and relative sensitivities for the different detector configurations are summarized in Table 3. The values are reported after rounding for argon and Xe–Ne gas mixtures. For each configuration, we list the square root of the expected background counts ($N_{b,i}^{1/2}$), the signal efficiency (ϵ_i), and the relative sensitivity ratio (R_i), where i indexes the BCA, Primakoff ($a\gamma$), and axion–nucleon (aN) channels. Since $N_{\gamma,i}$ is proportional to ϵ_i, we define the relative signal-to-noise ratio for each gas pressure configuration as

$$R_{i(j)} = \frac{\epsilon_{i(j)}/N_{b,i(j)}^{1/2}}{\epsilon_{i(0)}/N_{b,i(0)}^{1/2}} = \frac{\epsilon_{i(j)}N_{b,i(0)}^{1/2}}{\epsilon_{i(0)}N_{b,i(j)}^{1/2}}, \tag{3}$$

Table 2
Statistical summary of simulated cosmic-ray-induced events for the different Micromegas configurations with 3 cm and 6 cm drift regions. For each gas mixture (argon-based and xenon–neon-based) and pressure, the table lists the number of generated primary cosmic particles (neutrons and gammas) and the corresponding number of events producing energy deposition in the Micromegas detector. The percentages of the contributions are given separately according to the progenitor particle, namely neutron-induced and gamma-induced events, together with their total. The total number of events registered in the Micromegas is reported with its statistical uncertainty (in parentheses). Events depositing energy in the sensitive volume within the 0–20 keV range are distinguished from those depositing energy at higher energies.

		3 cm drift						
		Cosmic	Micromegas Events			Micromegas Events		
	$P_{(bar)}$	$(n+\gamma)$	$(n)_{primary}$	$(\gamma)_{primary}$	$(n+\gamma)_{primary}$	$(n)_{primary}$	$(\gamma)_{primary}$	$(n+\gamma)_{primary}$
			Energy range between 0 and 20 keV			Energy range above 20 keV		
Argon	1.2	81 146 062	58.4%	0.6%	7082 (84)	40.7%	0.3%	4919 (70)
	1.5	80 059 211	50.1%	0.5%	6068 (78)	49.0%	0.4%	5932 (77)
	2.0	75 491 677	41.9%	0.5%	5092 (71)	57.2%	0.4%	6909 (63)
Xe-Ne	1.05	63 740 313	50.5%	0.5%	6121 (78)	48.5%	0.5%	5880 (77)
	1.5	57 154 565	41.9%	0.4%	5073 (71)	57.2%	0.5%	6928 (83)
	2.0	49 650 429	35.0%	0.4%	4244 (65)	64.0%	0.6%	7756 (88)
		6 cm drift						
		Cosmic	Micromegas Events			Micromegas Events		
	$P_{(bar)}$	$(n+\gamma)$	$(n)_{primary}$	$(\gamma)_{primary}$	$(n+\gamma)_{primary}$	$(n)_{primary}$	$(\gamma)_{primary}$	$(n+\gamma)_{primary}$
			Energy range between 0 and 20 keV			Energy range above 20 keV		
Argon	1.2	56 229 392	44.7%	0.4%	5416 (74)	54.5%	0.4%	6584 (81)
	1.5	54 047 787	37.9%	0.3%	4592 (68)	61.4%	0.4%	7408 (86)
	2.0	49 832 969	28.9%	0.4%	3519 (59)	70.2%	0.5%	8483 (92)
Xe-Ne	1.05	41 379 462	39.6%	0.5%	4809 (69)	59.4%	0.5%	7193 (85)
	1.5	35 248 430	34.2%	0.3%	4136 (64)	65.0%	0.5%	7864 (89)
	2.0	31 055 962	31.8%	0.3%	3857 (62)	67.4%	0.5%	8143 (90)

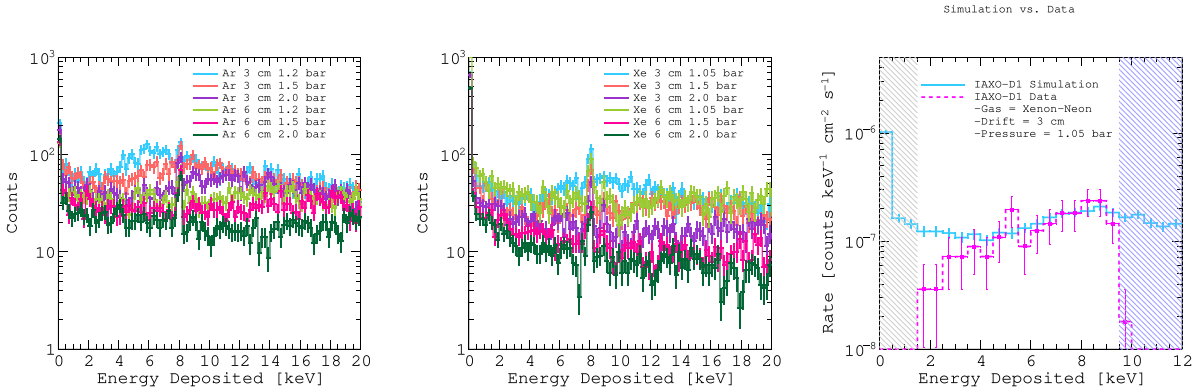

Fig. 15. Energy spectra of events depositing energy in the different Micromegas detector configurations for argon-based (left) and xenon–neon-based (center) gas mixtures. The distributions represent the energy deposited in the detector by events generated within the simulated energy range of primary particles (see Fig. 13). The simulated spectra include all energy depositions occurring in the sensitive volume of IAXO-D1, independent of the progenitor particle type (neutron- or gamma-induced). Additionally, a comparison is shown between Xe–Ne experimental data from IAXO-D1 at 1.05 bar with a 3 cm drift chamber (magenta histogram) and simulated data produced by our routines (cyan histogram). The experimental data histogram is adapted from [24], assuming full efficiency of a muon-veto discrimination. The region shaded in gray indicates the energy range below the detector threshold, while the region shaded in blue corresponds to energies outside the dynamic range of the electronics used by IAXO-D1 during the data taking.

where the index j runs over the different gas mixtures and pressure configurations. The reference case ($j = 0$) corresponds to argon at 1.2 bar with a 3 cm drift chamber. The uncertainties on the signal-to-noise ratio are also reported in the table. These include both the statistical uncertainties from the integrated efficiency over the energy range and the statistical uncertainties associated with the simulated background counts. The latter are estimated as the standard deviation of the number of background counts obtained from simulations with identical configurations.

Energy spectra of events depositing energy in the Micromegas sensitive volume are shown in Fig. 15 for the argon (left) and xenon–neon (center) gas mixtures. These spectra represent the total energy deposited by all simulated cosmic-ray-induced interactions, including both neutron and gamma contributions. In Fig. 15 (right), we compare Xe–Ne simulated spectra with experimental data obtained with the IAXO-D1 detector that was reported in [24]. In this particular plot, the region shaded in gray indicates energies below the detector threshold. This threshold is primarily determined by the 4 μm aluminized Mylar window, which defines the minimum energy of X-rays that can penetrate into the gas volume of the Micromegas detector. The region shaded in blue corresponds to energies outside the dynamic range of the IAXO-D1 electronics during data taking. In practice, the readout electronics also imposed a minimum detectable energy of approximately 1.5 keV. Events below this energy are not reliably recorded, defining the effective electronic threshold for the measurement. The measurements were performed with a multilayer veto system designed to tag cosmic-ray-induced muons. The dataset corresponds to an effective exposure time of 52 days and achieved a background level of 8.6×10^{-7} counts $\mathrm{keV}^{-1}\,\mathrm{cm}^{-2}\,\mathrm{s}^{-1}$, representing

Table 3
Summary of the simulated detector performance for argon and Xe–Ne gas mixtures at different pressures and two drift lengths (3 cm and 6 cm). For each configuration the square root of the expected background counts ($N_b^{1/2}$), the signal efficiency (ϵ), and the relative sensitivity ratio (R) are reported for three signal channels: BCA, Primakoff conversion ($a\gamma$), and axion–nucleon interaction (aN). The quantities are evaluated in the corresponding energy windows: 0.5–4.0 keV (BCA), 2–7 keV ($a\gamma$), and 12–17 keV (aN). Sensitivity ratios are normalized to the reference configuration of argon at 1.2 bar and 3 cm drift.

	3 cm drift									
	$P_{(bar)}$	$N^{1/2}_{b,BCA}$	$\epsilon_{BCA(\%)}$	R_{BCA}	$N^{1/2}_{b,a\gamma}$	$\epsilon_{a\gamma(\%)}$	$R_{a\gamma}$	$N^{1/2}_{b,aN}$	$\epsilon_{aN(\%)}$	R_{aN}
Argon	1.2	32.20	0.45	1.00 (0.02)	46.15	0.78	1.00 (0.02)	37.42	0.11	1.00 (0.01)
	1.5	31.19	0.47	1.07 (0.03)	38.81	0.82	1.25 (0.02)	36.74	0.14	1.27 (0.02)
	2.0	29.81	0.48	1.16 (0.03)	34.26	0.87	1.49 (0.03)	38.61	0.18	1.59 (0.02)
Xe-Ne	1.05	38.02	0.50	0.94 (0.02)	44.56	0.91	1.21 (0.02)	42.83	0.39	3.12 (0.05)
	1.5	39.63	0.50	0.91 (0.02)	43.13	0.93	1.27 (0.02)	46.77	0.51	3.74 (0.05)
	2.0	44.46	0.50	0.81 (0.02)	47.59	0.93	1.15 (0.02)	41.99	0.61	5.03 (0.07)
		BCA			Primakoff			axion–nucleon		
	6 cm drift									
	$P_{(bar)}$	$N^{1/2}_{b,BCA}$	$\epsilon_{BCA(\%)}$	R_{BCA}	$N^{1/2}_{b,a\gamma}$	$\epsilon_{a\gamma(\%)}$	$R_{a\gamma}$	$N^{1/2}_{b,aN}$	$\epsilon_{aN(\%)}$	R_{aN}
Argon	1.2	42.93	0.49	0.81 (0.02)	50.41	0.88	1.03 (0.02)	54.55	0.21	1.33 (0.02)
	1.5	41.93	0.50	0.84 (0.02)	48.28	0.90	1.10 (0.02)	50.22	0.26	1.77 (0.03)
	2.0	42.56	0.50	0.84 (0.02)	48.74	0.91	1.11 (0.02)	42.71	0.33	2.67 (0.04)
Xe-Ne	1.05	56.19	0.50	0.64 (0.02)	59.58	0.93	0.92 (0.02)	57.71	0.63	3.76 (0.05)
	1.5	65.52	0.50	0.55 (0.01)	69.14	0.93	0.80 (0.02)	53.99	0.76	4.84 (0.07)
	2.0	70.79	0.51	0.51 (0.01)	71.84	0.93	0.77 (0.01)	57.78	0.85	5.06 (0.07)
		BCA			Primakoff			axion–nucleon		

the lowest background reported for this type of detector with above-ground conditions. The simulated spectra reproduce the main features observed in the experimental data [24]. In particular, they capture the continuous background component. To enable a direct comparison, the simulated distributions were normalized by matching the intensity of the copper fluorescence line taking into consideration the energy resolution achieved by IAXO-D1 during the data taking. This procedure compensates for differences in absolute event rates between simulation and data while preserving the spectral shape. After normalization, the simulated spectra (shown in blue) follow the general trend of the measured distribution across the considered energy range (shown in magenta), with remaining differences compatible with the statistical uncertainties of the dataset.

The residual discrepancies between simulation and measurement can be largely attributed to differences in the analysis selections. In the experimental dataset, a fiducial radius of 9 mm was applied, restricting the analysis to the central region of the detector, while our simulations include the entire drift volume, which increases the contribution from low energy events occurring near the detector boundaries.

5. Conclusions

The primary objective of this study was to investigate and enhance the nominal sensitivity of IAXO's Micromegas detectors to various solar axion couplings, with particular focus on the axion–nucleon interaction. This goal was systematically pursued through a comprehensive exploration of alternative configurations of the IAXO-D1 prototype. Potential performance enhancements were assessed by increasing the operating pressure, extending the drift length to 6 cm, and exploring different gas mixtures. In addition, the impact of cosmic-induced background was evaluated for each configuration to ensure a realistic assessment of detector performance.

Within the engineering limitations of IAXO-D1, the adoption of a Xe–Ne–isobutane gas mixture, fully compatible with the existing IAXO-D1 design, demonstrates superior performance compared to any argon-based configuration. Notably, this improvement is achieved without requiring structural modifications, such as changes to the drift distance. The proposed mixture results in a substantial enhancement in axion–nucleon sensitivity, increasing the signal-to-noise ratio by nearly a factor of 3.1 to 3.7.

Further improvements could be achieved by overcoming the limitations imposed by the detector's energy threshold. This requires the development of a new cathode window with enhanced transparency for photons below ∼1 keV, which is currently under engineering. In conclusion, this study establishes a clear framework for reaching the targeted axion–nucleon sensitivity in future upgrades of the IAXO-D1 prototype and for enhancing the overall Micromegas detector response to axion–nucleon interactions.

The data and code that support the findings of this article are openly available in [25].

CRediT authorship contribution statement

I. Antolín: Visualization, Software, Investigation, Formal analysis. **J.F. Castel:** Validation, Methodology, Investigation. **T. Dafni:** Validation, Methodology. **E. Ferrer-Ribas:** Validation, Methodology. **J. Galán:** Validation, Methodology. **A. Huerva:** Visualization, Software, Investigation, Formal analysis, Data curation. **I.G. Irastorza:** Validation, Methodology, Investigation. **G. Luzón:** Validation, Methodology. **C. Margalejo:** Writing – review & editing, Validation, Supervision, Software, Investigation, Formal analysis, Data curation. **H. Mirallas:** Validation, Methodology. **L. Obis:** Validation, Software, Methodology. **J. Porrón:** Validation, Methodology, Investigation. **M.J. Puyuelo:** Validation, Software, Methodology. **J. Ruz:** Writing – review & editing, Writing – original draft, Visualization, Validation, Supervision, Software, Project administration, Methodology, Investigation, Funding acquisition, Formal analysis, Data curation, Conceptualization. **J.K. Vogel:** Validation, Resources, Methodology, Funding acquisition.

Declaration of competing interest

The authors declare that they have no known competing financial interests or personal relationships that could have appeared to influence the work reported in this paper.

Acknowledgments

We acknowledge support from the Spanish Agencia Nacional de Investigación (AEI) under grants PID2019-108122GB-C31 and PID2022-137268NB-C51, as well as the "Planes complementarios, Programa de Astrofísica *y* Física de Altas Energías" from the "European Union

NextGenerationEU/PRTR" funds; the European Research Council (ERC) under grant ERC 802836; and the Agence Nationale de la Recherche (France) ANR-19-CE31-133 0024. This project received funding from the Erasmus+ Programme of the European Union.

Data availability

The data and code that support the findings of this article are openly available in ref. 25 of the manuscript.

References

[1] R.D. Peccei, H.R. Quinn, CP conservation in the presence of pseudoparticles, Phys. Rev. Lett. 38 (1977) 1440.
[2] R.D. Peccei, H.R. Quinn, Constraints imposed by CP conservation in the presence of pseudoparticles, Phys. Rev. D 16 (1977) 1791.
[3] D.F.J. Kimball, K. van Bibber, The Search for Ultralight Bosonic Dark Matter, Springer Nature, 2023.
[4] A.B. Aleksandrov, et al., Search for weakly interacting massive dark matter particles: state of the art and prospects, Phys.-Usp. 64 (9) (2021) 861.
[5] I.G. Irastorza, et al., Future axion searches with the International Axion Observatory (IAXO), 2013.
[6] V. Anastassopoulos, et al., New CAST limit on the axion–photon interaction, Nat. Phys. 13 (2017) 584.
[7] K. Altenmüller, et al., New upper limit on the axion-photon coupling with an extended CAST run with a xe-based micromegas detector, Phys. Rev. Lett. 133 (2024) 221005.
[8] K. Zioutas, et al., Axion searches with helioscopes and astrophysical signatures for axion(-like) particles, New J. Phys. 11 (2009) 105020.
[9] P. Sikivie, Dark matter axions, Int. J. Mod. Phys. A 25 (02n3) (2010).
[10] P. Sikivie, Particle physics and cosmology: Dark matter, Phys. Rev. Lett. 51 (1984) 1415.
[11] K. van Bibber, et al., Design for a practical laboratory detector for solar axions, Phys. Rev. D 39 (1989) 2089.
[12] S. Hoof, J. Jaeckel, L.J. Thormaehlen, Quantifying uncertainties in the solar axion flux and their impact on determining axion model parameters, J. Cosmol. Astropart. Phys. 09 (2021) 006.
[13] P. Carenza, M. Giannotti, J. Isern, A. Mirizzi, O. Straniero, Axion astrophysics, Phys. Rep. 1117 (2025) 1–102.
[14] S. Andriamonje, et al., Search for 14.4 keV solar axions emitted in the M1-transition of 57Fe nuclei with CAST, J. Cosmol. Astropart. Phys. 12 (2009) 002.
[15] Di Luzio, et al., Probing the axion–nucleon coupling with the next generation of axion helioscopes, Eur. Phys. J. C 82 (2022) 120.
[16] K. Barth, et al., CAST constraints on the axion-electron coupling, J. Cosmol. Astropart. Phys. 05 (2013) 010.
[17] J. Redondo, Solar axion flux from the axion-electron coupling, J. Cosmol. Astropart. Phys. 12 (2013).
[18] E. Armengaud, et al., Physics potential of the international axion observatory, J. Cosmol. Astropart. Phys. 06 (2019) 047.
[19] Luca Di Luzio, et al., Stellar evolution confronts axion models, J. Cosmol. Astropart. Phys. 02 (2022) 035.
[20] A. Abeln, et al., Conceptual design of BabyIAXO, the intermediate stage towards the International Axion Observatory, J. High Energy Phys. 05 (2021) 137.
[21] S. Andriamonje, et al., Development and performance of Microbulk Micromegas detectors, J. Instrum. 5 (2010) P02001.
[22] E. Ruiz-Chóliz, Ultra-low Background Micromegas X-ray Detectors for Axion Searches in IAXO and BabyIAXO (Ph.D. thesis), University of Zaragoza (Spain), 2019.
[23] A. Quintana, et al., Spatial resolution studies with the BabyIAXO Micromegas prototype, Nucl. Instrum. Methods A 1083 (2026) 171176.
[24] K. Altenmüller, et al., Background discrimination with a Micromegas detector prototype and veto system for BabyIAXO, Front. Phys. Vol. 12 (2024) 1384415.
[25] Repository with data analysis and code, https://github.com/AHuerva/Axion-Nucleon_Sensitivity_Study/.
[26] K. Altenmuller, et al., REST-for-Physics, a ROOT-based framework for event oriented data analysis and combined Monte Carlo response, Comput. Phys. Comm. 273 (2022) 108281.
[27] J. Allison, et al., Recent developments in Geant4, Nucl. Instrum. Methods A 835 (2016) 186–225.
[28] IAXO github, https://github.com/iaxo.
[29] A.C. Thomson, X-ray Data Booklet, https://books.google.es/books?id=WV05HAAACAAJ.
[30] K. Altenmüller, et al., Search for solar axions produced through the axion-electron coupling g_{ae} using a new GridPix detector at CAST, J. High Energ. Phys. 2025 (2025) 9.
[31] L. Lista, Statistical Methods for Data Analysis, Springer, 2017.
[32] A.L. MacKinnon, I.J. D Craig, Stochastic simulation of fast particle diffusive transport, Astron. Astrophys. 251 (2) (1991) 693–699.
[33] S.F. Biagi, Magboltz Simulation Program, https://magboltz.web.cern.ch/magboltz/.
[34] H. Schindler, R. Veenhof, Garfield++ Program, https://gitlab.cern.ch/garfield/garfieldpp.
[35] J. Galan, et al., Topological background discrimination in the PandaX-III neutrinoless double beta decay experiment, J. Phys. G: Nucl. Part. Phys. 47 (2020) 045108.
[36] C. Hangman, et al., Monte Carlo Simulation of Proton-Induced Cosmic Ray Cascades in the Atmosphere, Technical Report UCRL-TR-229452, Lawrence Livermore National Laboratory, 2007.
[37] D. Autiero, et al., The CAST time projection chamber, New J. Phys. 9 (2007) 171.
[38] G. Luzón, et al., Background studies and shielding effects for the TPC detector of the CAST experiment, New J. Phys. 9 (2007) 208.
[39] J.G. Garza, et al., Low background micromegas in CAST, J. Phys.: Conf. Ser. 650 (2015) 012008.
[40] E. Ferrer-Ribas, et al., Ultra low background Micromegas detectors for BabyIAXO solar axion search, J. Instrum. 18 (2023) C10003.
[41] J. Castel, et al., Improvement and assessment of the radiopurity of Micromegas readout planes, arXiv:2603.03274.
[42] K. Altenmüller, et al., Alphacamm, a micromegas-based camera for high-sensitivity screening of alpha surface contamination, J. Instrum. 17 (2022) P08035.
[43] Jackson Kimball Derek F, Karl van Bibber, The Search for Ultralight Bosonic Dark Matter, Springer International Publishing, Cham, 2022, ISBN: 978-3-030-95851-0 (hardcover); ISBN: 978-3-030-95852-7 (eBook).